Published July 25, 2019

Original Research

Core Ideas

- A triaxial apparatus is developed to measure stress-dependent SFCC.
- Unfrozen water content of clay and sand increases with increasing confining stress.
- Stress effects on the SFCC of clay are more significant than sand.

Stress Effects on Soil Freezing Characteristic Curve: Equipment Development and Experimental Results

Q.Y. Mu, C. Zhou,* C.W.W. Ng, and G.G.D. Zhou

The soil freezing characteristic curve (SFCC) defines the relationship between soil temperature and unfrozen water content. This curve is important for predicting water flow and heat conduction in frozen soils, as well as freezing heave and thawing settlement. So far, SFCCs reported in the literature were usually determined at zero stress. To investigate stress effects on SFCC, a stress- and temperature-controlled triaxial apparatus was developed in this study. The unfrozen volumetric water content was measured using a newly developed noninvasive time domain reflectometry (TDR) probe. The new apparatus was used to measure SFCCs of two typical soils (i.e., clay and sand) at different stress conditions (i.e., 30, 100, and 200 kPa). Each specimen was subjected to compression, and then a cycle of freezing and thawing. As expected, for both soils, the saturated water content prior to freezing was smaller at higher stresses because of compression. During the subsequent freezing and thawing, the soil specimen at a higher stress was able to retain more liquid water than that at a lower stress. The higher unfrozen water retention capacity at higher stresses is mainly because the pore size of a soil specimen becomes smaller during compression. Hence, more water can retain a liquid state due to the enhanced capillarity. On the other hand, stress effects on the SFCC were found to be more significant for clay than for sand. This is likely because the stress-induced change in pore size distribution is larger in clay due to its higher compressibility.

Abbreviations: NMR, nuclear magnetic resonance; SFCC, soil freezing characteristic curve; TDR, time domain reflectometry.

Q.Y. Mu, Dep. of Civil Engineering, Xi'an Jiaotong Univ., Xi'an, P.R. China; C. Zhou, Dep. of Civil and Environmental Engineering, Hong Kong Polytechnic Univ., Hung Hom, Hong Kong; C.W.W. Ng, Dep. of Civil and Environmental Engineering, Hong Kong Univ. of Science and Technology, Clear Water Bay, Kowloon, Hong Kong; G.G.D. Zhou, Key Lab. of Mountain Hazards and Earth Surface Process/Institute of Mountain Hazards and Environment, Chinese Academy of Sciences (CAS), Chengdu, P.R. China. *Corresponding author (c.zhou@polyu.edu.hk).

Received 16 Nov. 2018.
Accepted 30 May 2019.

Citation: Mu, Q.Y., C. Zhou, C.W.W. Ng, and G.G.D. Zhou. 2019. Stress effects on soil freezing characteristic curve: Equipment development and experimental results. Vadose Zone J. 18:180199. doi:10.2136/vzj2018.11.0199

Soils are subjected to daily and seasonal variation in the field (Zhou and Ng, 2016). When the temperature is below 0°C, some pore water is still able to retain a liquid state. This is due to the freezing point depression attributed to the surface tension at the ice–water interface (Spaans and Baker, 1995, Zhou et al., 2018). According to Kelvin's equation, the freezing point depression is more significant when the radius of ice–water interface is smaller (Lebeau and Konrad, 2012; Mu et al., 2018). The relationship between temperature and unfrozen water content is defined as the soil freezing characteristic curve (SFCC). A good understanding of SFCC is of primary importance for studying water flow and heat conduction in frozen soils (Flerchinger et al., 2006), as well as freezing heave and thawing settlement of the ground (Zhang and Michalowski, 2015). On the other hand, soils are usually subjected to various stress conditions in the field, affecting pore structure (Ng and Pang, 2000; Zhou and Ng, 2014) and thus SFCC. Konrad (1990) and Azmatch et al. (2012) studied effects of stress history on SFCC. In their tests, soil specimens were first loaded and then unloaded to zero stress. They found that after a cycle of loading and unloading, the soil specimen was able to retain more water in a liquid state during freezing (i.e., a higher retention capability of unfrozen water). It should be noted that all of the above SFCCs were determined at zero stress. To fully understand the effects of stress on SFCC, it would be necessary to maintain a nonzero stress during freezing and thawing.

In an SFCC test, unfrozen water content is generally determined through either nuclear magnetic resonance (NMR) (Watanabe and Wake, 2009, Tian et al., 2017) or time domain reflectometry (TDR) (Spaans and Baker, 1995; Bittelli et al., 2003; He and Dyck, 2013; Tian et al., 2015). The TDR method is popular because it is low cost and can

be used to obtain continuous measurements easily. Currently, the widely used TDR probe is invasive, with three steel rods (about 4–8 mm in diameter and 100–200 mm in length) inserted in soil specimen during the test (Spaans and Baker, 1995; Watanabe and Wake, 2009; He and Dyck, 2013; Tian et al., 2015). With three steel rods in soil, it is very difficult to control uniform stress distribution within a soil specimen. Bittelli et al. (2003) developed a thermodielectric analyzer that includes a noninvasive TDR probe and a thermistor. During freezing and thawing, the SFCC could be determined by simultaneously measuring the soil unfrozen volumetric water content and temperature through the noninvasive TDR probe and the thermistor, respectively. However, accurate control of soil stress state is unavailable with the thermodielectric analyzer. It is therefore necessary to develop a new apparatus for measuring SFCC with the following features: (i) accurate measurement of unfrozen water content, (ii) control of uniform soil stress, and (iii) high-quality of temperature control.

In this study, a new triaxial apparatus was developed for measuring stress-dependent SFCC. The newly developed apparatus was modified from a conventional triaxial cell by adding a noninvasive TDR probe and a temperature control system. The performance of the new triaxial apparatus is demonstrated by testing two typical soils (i.e., clay and sand) at different confining stresses. These measurements are interpreted to reveal stress effects on SFCC.

Description of the Newly Developed Triaxial Apparatus

Figure 1 shows a schematic diagram of the new triaxial apparatus. The device consists of a noninvasive TDR probe, a temperature control system, and a conventional Global Digital Systems triaxial cell. The non-invasive TDR probe is used to measure soil unfrozen volumetric water content. Its design and calibrations are described in detail in the Noninvasive TDR Probe section below. The temperature control system consists of a thermostat, a pump, a bath, a spiral tube, antifreeze liquid, and rubber insulation cotton. The working principle and verification of the temperature control system are described in the Temperature Control System section below. In addition, the conventional triaxial cell consists of an acrylic chamber, an advanced Global Digital System pressure controller for controlling confining pressure, and a loading frame for controlling deviator stress.

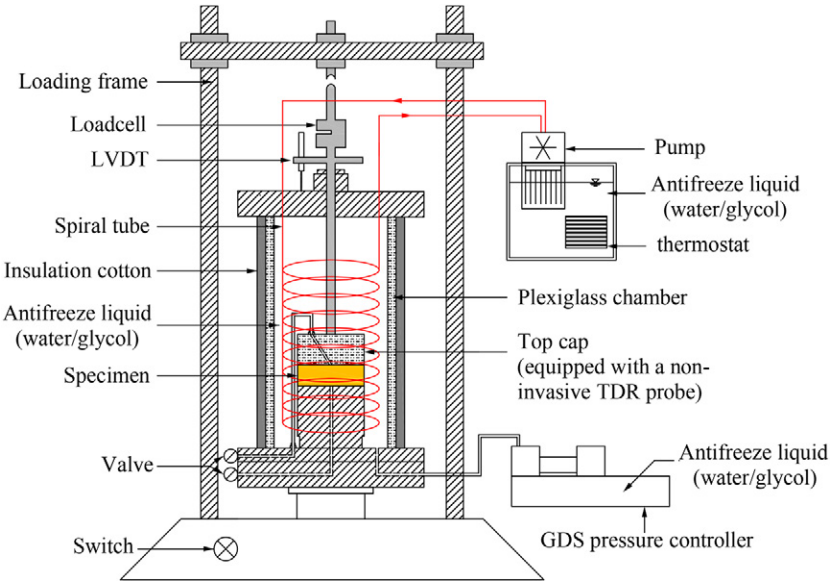

Fig. 1. Schematic diagram of the new triaxial apparatus for measuring stress-dependent soil freezing characteristic curve (SFCC). LVDT stands for a linear variable differential transformer, TDR stands for time domain reflectometry, and GDS stands for Global Digital Systems.

Noninvasive Time Domain Reflectometry Probe

Design of the Probe

Figure 2 shows the schematic diagram of the noninvasive TDR probe. A circular groove is produced on the top cap where the noninvasive TDR probe is embedded. During testing, the top cap equipped with the noninvasive TDR probe was placed on top of the specimen to sense the soil medium. The noninvasive TDR probe was produced from a metal-coated printed circuit board (Nissen et al., 2003). Three parallel copper plates are positioned on the surface of a circuit laminate to form a transmission line. To ensure a sufficient length of the transmission line, the copper plates are configured in a serpentine pattern similar to the design proposed by Selker et al. (1993). The separation between neighboring copper plates is 5 mm. For each copper plate, the thickness and width are 0.02 and 1 mm, respectively. Furthermore, the circuit laminate with a thickness of 6 mm was chosen to ensure that the sample area of the noninvasive TDR probe is independent of the dielectric permittivity of the circuit laminate and the surrounding soil (detailed discussion is shown below). In addition, the noninvasive TDR probe is connected to a coaxial cable (impedance = 50 Ω) by soldering. The center conductor of the coaxial cable is soldered to the center copper plate, whereas the shield is soldered to the two outer copper plates.

Theory for Quantifying the Sample Area

The sample area of a TDR probe significantly affects the accuracy of water content measurements. This is because water and soil particle distributions within a soil specimen are highly heterogeneous. The sample area should be large enough to ensure that the water content within this area can represent the water content of the whole specimen. The sample area of TDR probe could be determined using the electromagnetic theory and the numerical method proposed by Knight (1992) and Ferré et al. (1998). According to Knight (1992), the weighting factor $[w(x, y)]$ was used to quantify the measurement sensitivity of the proposed noninvasive TDR probe in the plane perpendicular to the wave propagation.

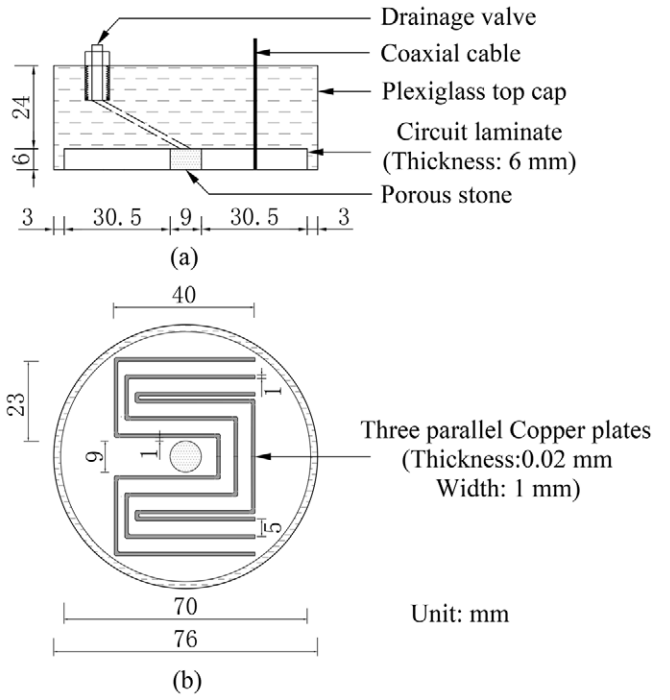

Fig. 2. Schematic diagram of the noninvasive time domain reflectometry (TDR) probe installed in the top cap: (a) cross-sectional view and (b) plane view.

$$w(x,y)=\frac{\nabla\Phi^2(x,y)}{\iint_\Omega \nabla\Phi_o^2(x,y)\mathrm{d}x\mathrm{d}y} \quad [1]$$

where $\Phi(x, y)$ is the electrostatic potential in the heterogeneous $\varepsilon(x, y)$ field and $\Phi_o(x, y)$ is the electrical potential in the case of a uniform ε_o field. To compute the distributions of $\Phi(x, y)$ and $\Phi_o(x, y)$, the following Laplace equation should be solved (Zhan et al., 2013):

$$\nabla\left[\varepsilon(x,y)\nabla\Phi(x,y)\right]=0 \quad [2]$$

This equation is very similar to the governing equation for the steady state water flow within the saturated porous material:

$$\nabla\left[K(x,y)\nabla H(x,y)\right]=0 \quad [3]$$

where $K(x, y)$ and $H(x, y)$ are the permeability coefficient and the hydraulic head, respectively. It is clear that the $\varepsilon(x,y)$ and the $\Phi(x,y)$ in Eq. [2] correspond to the $K(x,y)$ and the $H(x,y)$ in Eq. [3], respectively. Hence, a finite element software (e.g., Geostudio) for calculating $H(x,y)$ was used here to determine the distribution of $\Phi(x,y)$.

It should be noted that Eq. [1] is used to quantify the measurement sensitivity of each point surrounding the noninvasive TDR probe. This distribution of measurement sensitivity is adopted to determine the sample area of the noninvasive TDR probe, on the basis of a parameter f introduced by Ferré et al. (1998):

$$f=\frac{100\%\sum_{w_{hi}}^{w} w_i A_i}{\iint w_i \mathrm{d}A} \quad [4]$$

where w and A define the measurement sensitivity and research area, respectively, w_i is the measurement sensitivity of the ith finite element, A_i is the area of the element, and w_{hi} represents the largest value of w_i. On the right hand side of Eq. [4], the numerator is calculated by summing the product of w_i and A_i, starting with those elements with the highest w_i and progressively decreasing w_i. The denominator is the summation of the product of w_i and A_i for all elements. Following this definition, f is a function of w_i, and its value ranges from 0 to 100%. When f reaches 90%, all the elements considered in the calculation of numerator form the sample area (Zhan et al., 2015).

Numerical Studies for Calculating the Sample Area

According to the above theoretical analysis, numerical studies were performed to determine the sample area of the proposed noninvasive TDR probe in the plane perpendicular to the wave propagation. Figure 3 illustrates the numerical model for computing the electrostatic potential around the noninvasive TDR probe

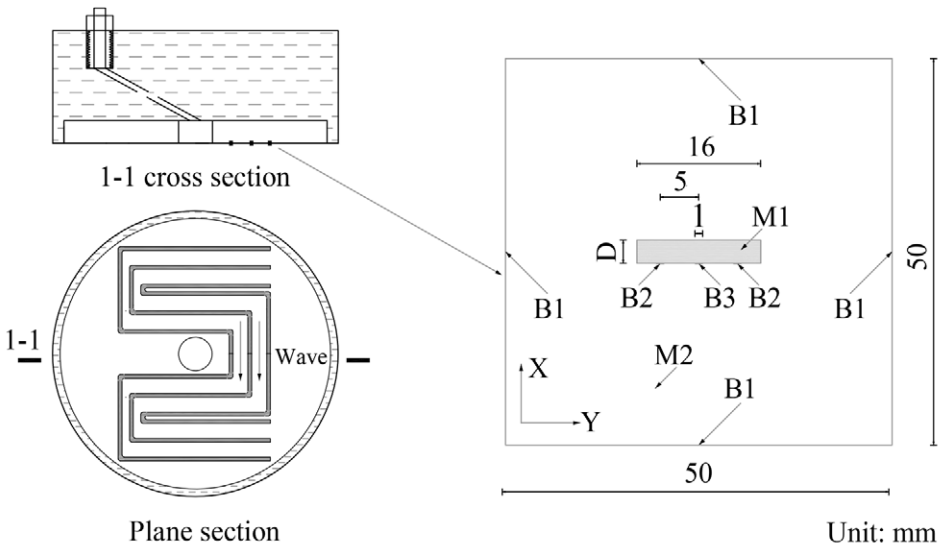

Fig. 3. Illustration of the numerical model for computing the electrostatic potential field in the plane perpendicular to the wave propagation.

in the plane perpendicular to the wave propagation. The variable D represents the thickness of the circuit laminate. The value of D was set to 1.5, 3.0, and 6.0 mm. Other dimensions such as the separation of the copper plate and the height and width of the copper plate were the same as those described above. The variables M1 and M2 represent the material of circuit laminate and the target medium, respectively. In this study, the permeability coefficient of M1 was set as 1 and 80, which represent the dielectric permittivity of air ($\varepsilon = 1$) and water ($\varepsilon = 80$), respectively. The permeability coefficient of M_2 was set as 3.5, corresponding to the measured dielectric permittivity of the circuit laminate. On the other hand, B1, B2, and B3 represent the boundary conditions. For the seepage analysis, B2 and B3 were set as a constant hydraulic head of $H = -1$ and $H = 1$ respectively, which correspond to a constant electric potential of $\Phi = -1$ and $\Phi = 1$. As the research region is large enough to cover the whole sample area of the noninvasive TDR probe, the boundary of B_1 was set as a zero-flow condition (i.e., $\partial H/\partial \overline{n} = 0$).

Figure 4 shows the sample area in the plane perpendicular to the wave propagation (i.e., cross-sectional plane 1–1 in Fig. 3) with three different thicknesses of laminate circuit. Figure 4a shows the sample area of the noninvasive TDR probe with a circuit laminate thickness of 1.5 mm. For a probe surrounded by a medium with a dielectric permittivity of 1, the sample area penetrates beyond the upper boundary of the circuit laminate and extends into the medium above. The sample area can be represented as an ellipse with a semimajor axis of 6 mm and a semiminor axis of 3.5 mm. As the dielectric permittivity of the surrounding medium increases from 1 to 80, the distance between the upper boundary of the sample area and the circuit laminate decreases from 3.6 to 2.3 mm. Furthermore, none of the sample area penetrates into the medium above the circuit laminate. It is clear that the sample area decreases significantly as the dielectric permittivity of the surrounding medium increases.

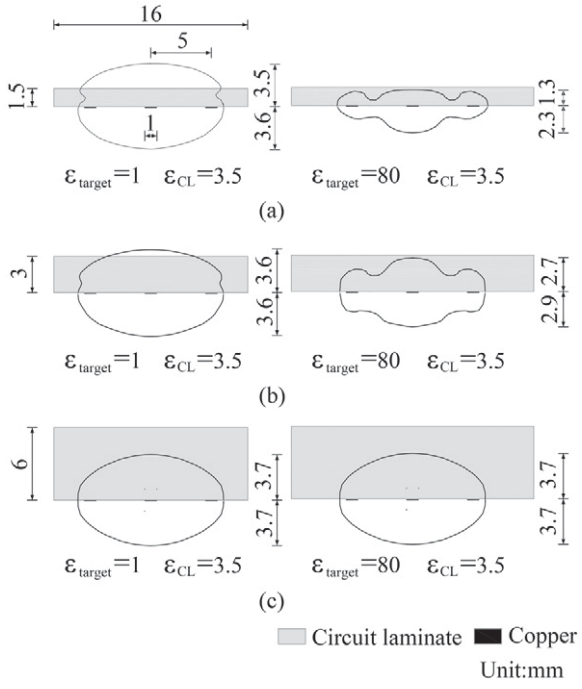

Fig. 4. Sample area of the noninvasive time domain reflectometry (TDR) probe with laminate circuit thickness of (a) 1.5 mm, (b) 3 mm, and (c) 6 mm. ε_{target} is the dielectric permittivity of target material, and ε_{CL} is the dielectric permittivity of circuit laminate.

Figure 4b shows the sample area of the noninvasive TDR probe with a circuit laminate thickness of 3 mm. For a probe surrounded by a medium with a dielectric permittivity of 1, an elliptical sample area with a semimajor axis of 6 mm and a semiminor axis of 3.6 mm is obtained. The sample area decreases significantly as the dielectric permittivity of the surrounding medium increases from 1 to 80, similar to the probe with a circuit laminate thickness of 1.5 mm. More importantly, the sample area of the probe with a circuit laminate thickness of 3 mm is ~1.5 times larger than that of the probe with a circuit laminate thickness of 1.5 mm.

Figure 4c shows the sample area of the noninvasive TDR probe with a circuit laminate thickness of 6 mm. Here, the sample area is evenly distributed between the circuit laminate and the surrounding medium. The distribution of the sample area shows a pattern similar to the sample area obtained using the probes with a circuit laminate thickness of 1.5 and 3 mm. Furthermore, the sample area is constant as the dielectric permittivity of the surrounding medium increases from 1 to 80. Thus, the sample area is independent of the dielectric permittivity of the circuit laminate and the surrounding medium when using a circuit laminate thickness of 6 mm. With such a TDR probe, a linear calibration relationship between the effective dielectric permittivity measured by the noninvasive TDR probe and the dielectric permittivity of the surrounding material can be obtained (Zhan et al., 2015). The determination of water content using a probe with a constant sample area is expected to be more accurate than measurements conducted with probes with a circuit thickness of 1.5 or 3 mm. Therefore, the thickness of the circuit laminate used for this study was 6 mm.

To ensure that the measurement of a TDR probe can represent the average unfrozen water content of the soil specimen, the sample volume should be larger than the representative element volume, V_{sv}. According to some previous studies (Razavi et al., 2006; Al-Raoush and Papadopoulos, 2010), V_{sv} is about 20,000 times V_{D50}, which is the volume of a sphere with a diameter equal to the mean diameter of soil particles. In this study, the sampling size of the noninvasive TDR probe has a diameter of ~76 mm and a height of ~4 mm (see Fig. 4c). The ratios of the sample volume and V_{D50} of clay and sand are around 1.0×10^{10} and 5×10^{5}, respectively. Hence, the measurement of the noninvasive TDR probe may be considered to represent the average water content of the whole specimen.

Calibration of the Proposed Probe

Calibration for Measuring the Soil Dielectric Permittivity

The dielectric permittivity measured by the noninvasive TDR probe is an effective dielectric permittivity (ε_{eff}), which

is a weighted average of the soil dielectric permittivity (ε_{soil}) and the dielectric permittivity of the circuit laminate (ε_{cl}). To obtain ε_{soil} from the measured ε_{eff}, the calibration equation based on the homogenization model proposed by Birchak et al. (1974) was used:

$$(\varepsilon_{eff})^m = a(\varepsilon_{soil})^m + (1-a)(\varepsilon_{cl})^m \quad [5]$$

where m is a parameter that reflects the geometry of the medium with respect to the applied electric field, and a is a constant representing the weighting factor of the soil medium. It should be noted that the measured dielectric permittivity is affected by the dielectric permittivity of soil and circuit laminate around the waveguide. The ratio of soil dielectric permittivity to the measured dielectric permittivity is denoted by parameter a. For the noninvasive TDR probe designed in the current study, the sample areas in the soil and circuit laminate are symmetrical about the waveguide plane, as shown in Fig. 4c. Hence, soil and circuit laminate have identical contribution to the measured dielectric permittivity. The value of a is thus always equal to 0.5. On the other hand, the value of m ranges from −1 to 1, where m = 1 if the medium is a parallel connection of capacitors, and m = −1 for a series connection of capacitors (Lin et al., 2006). In this study, the soil and the circuit laminate were placed in parallel with the copper conductors in between (see Fig. 4c). Therefore, the value of m used for this work is 1. In addition, the measured value of ε_{cl} was 3.5.

Clay and sand specimens with different known water contents were used to calibrate the noninvasive TDR probe for measuring the soil dielectric permittivity. It should be noted that the TDR technique has a relatively low accuracy at low water contents. Furthermore, the amount of liquid water retained in the frozen soil is usually small. Therefore, the noninvasive TDR should be well calibrated at low water contents to obtain accurate measurements of unfrozen water content. In this study, 14 soil specimens with volumetric water content <20% were used to calibrate the relationship between ε_{soil} and the soil volumetric water content (θ_w). After specimen preparation, ε_{eff} was measured using the noninvasive TDR probe. A conventional three-rod TDR probe was subsequently inserted into the soil specimen to measure ε_{soil}. The calibrated relationships between ε_{eff} and ε_{soil} for clay and sand are shown in Fig. 5. The result shows good linear relationships, as proved by the high R^2 values (i.e., 0.99). The calibrated relationships provide equations to calculate ε_{soil} from the measured ε_{eff}:

$$\varepsilon_{soil} = \frac{\varepsilon_{eff} - 1.75}{0.5} \quad [6]$$

The measurement sensitivity of 0.5 is consistent with the numerical results (see Fig. 3c), showing that the sample area of the noninvasive TDR probe is evenly distributed through the circuit laminate and the soil. Therefore, the soil dielectric permittivity contributes 50% to the effective dielectric permittivity measured by the noninvasive TDR probe.

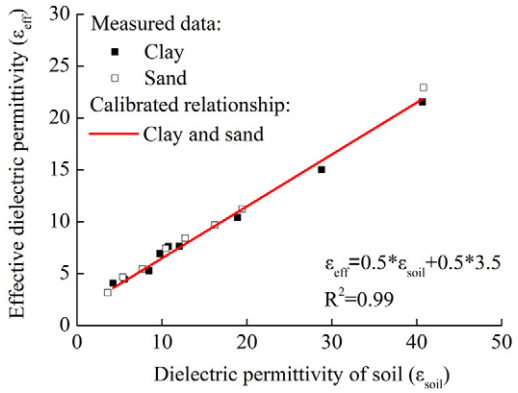

Fig. 5. Calibrated relationships between measured effective dielectric permittivity and dielectric permittivity for clay and sand.

Calibration for Measuring the Soil Unfrozen Volumetric Water Content

In the literature, functional relationships and composite model are widely used to correlate soil water content and dielectric permittivity. Some previous studies show that functional relationships are not applicable for unfrozen soil, mainly because that the dielectric permittivity of ice is different from the dielectric permittivity of air (Spaans and Baker, 1995; Seyfried and Murdock, 1996). In this study, the composite model proposed by Bittelli et al. (2003) was used, where the dielectric permittivity of ice and water, as well as their temperature dependence, can be accounted for. After obtaining the soil dielectric permittivity, the unfrozen volumetric water content was calculated by the composite model (Bittelli et al., 2003):

$$(\varepsilon_{soil})^k = (1-n)(\varepsilon_s)^k + \theta_w(\varepsilon_w)^k + \theta_i(\varepsilon_i)^k + (n-\theta_w-\theta_i)(\varepsilon_a)^k \quad [7]$$

where ε_s, ε_w, ε_i, and ε_a are the dielectric permittivity of soil matrix, air, liquid water, and ice, respectively, θ_w is the volumetric water content ($m^3\ m^{-3}$), θ_i is the volumetric ice content ($m^3\ m^{-3}$), n is the soil porosity, and k is a geometric factor. As mentioned above, the calibration tests were performed at room temperature (22 ± 1°C). Since no ice phase was present, Eq. [7] can instead be written as

$$\theta_w = \frac{(\varepsilon_{soil})^k - (1-n)(\varepsilon_s)^k - n(\varepsilon_a)^k}{(\varepsilon_w)^k - (\varepsilon_a)^k} \quad [8]$$

Figure 6 shows the calibration relationships between the volumetric water content and the dielectric permittivity of clay and sand. High values of R^2 (i.e., 0.97 and 0.98) are obtained for the calibration relationships. The values of parameter k are equal to 0.57 and 0.55 for clay and sand, respectively. In this study, the values of parameter k (i.e., 0.55 and 0.57) are similar to the calibration results of Roth et al. (1990), who suggested that a value of 0.5 for parameter k is appropriate to describe the composite model of different soils.

In the following experimental study, soil specimens were first completely saturated before freezing was applied to measure the

SFCC. The medium in the soil specimen thus consisted of the soil matrix, liquid water, and frozen water. This mixture allows Eq. [7] to be rewritten as

$$\theta_w = \frac{(\varepsilon_{soil})^{0.57} - (1-n)(\varepsilon_s)^{0.57} - n(\varepsilon_i)^{0.57}}{(\varepsilon_w)^{0.57} - (\varepsilon_i)^{0.57}} \quad [9]$$

Based on extensive calibration tests on 13 types of soils (including clay, sand, and silt at various densities), Roth et al. (1990) found that parameter k is independent of the soil type and soil density. The value of k is found to be controlled by the frequency and mode of electromagnetic field applied to the waveguide. Hence, it is reasonable to use the same k at different temperatures in the presence of ice. In the composite model, the temperature dependence of the dielectric permittivity of liquid water (ε_w) is accounted for by using equations and methods proposed by Archer and Wang (1990). On the other hand, thermal effects on the dielectric permittivity of ice (ε_i) are considered by using the empirical equation proposed by Bittelli et al. (2003):

$$\varepsilon_i(T) = 3.32 + 1.21 \times 10^{-2} T + 1.18 \times 10^{-3} T^2 + 5.2T^3 + 8.4 \times 10^{-7} T^4 \quad [10]$$

Temperature Control System

For the temperature control system, the antifreeze liquid is used to fill the bath and the triaxial cell (see Fig. 1). The temperature of the antifreeze liquid in the bath is controlled using the thermostat. Antifreeze liquid with a controlled initial temperature is circulated through a spiral tube that runs around the soil specimen. Soil specimen is frozen or thawed through heat exchange with the circulating antifreeze liquid. To reduce energy loss and to minimize soil temperature fluctuations, the triaxial cell is insulated with rubber cotton that has a very low thermal conductivity (0.03 W m^{-1} K^{-1}) (see in Fig. 1).

Calibration tests using three thermocouples attached at the top (P1), middle (P2), and bottom (P3) of a dummy sample were performed to measure temperature uniformity and observe any measurement fluctuations in the new triaxial apparatus. Freezing and thawing were applied in steps of −5°C, with temperatures ranging from 20 to −20°C. The confining stress used in the triaxial cell was 30 and 200 kPa, values similar to those used during measurements of SFCCs of clay and sand specimens in the section below.

Figure 7 shows temperatures measured at the top (P1), middle (P2), and bottom (P3) of the dummy during freezing and thawing. The confining stress applied was 100 kPa. It is clear that the measured temperatures decrease at each temperature step during freezing and increase in the subsequent thawing process. For each temperature step, the temperatures reach equilibrium (soil temperature at the center is equal to the soil temperature at the boundary) after ~4 h. At the equilibrium state, a temperature fluctuation of ±0.2°C was observed. To further reduce the temperature fluctuation, a propeller can be installed inside the cell in future to promote uniform temperature by convection. On the other hand, the temperature at P2 takes approximately an additional 30 min until an equilibrium state is reached compared with temperatures measured at P1 and P3. This delay in the evolution of sample temperature is mainly attributed to the thermal diffusion process within the specimen. As the specimen tested is axially symmetric, the measured temperatures at P1, P2, and P3 demonstrate that the temperature is uniform within the specimen at the equilibrium state. Calibration tests at confining stresses of 30 and 200 kPa show similar results to those in Fig. 7, demonstrating the repeatability of the temperature control system.

Soil Type, Experimental Program, and Test Procedures

Test Soil Properties

The SFCC of both clay and sand specimens were measured in this study. The information about the physical properties of the test soils are given in Table 1. According to ASTM D 2487-11 (ASTM, 2011), the clay and sand are classified as lean clay (CL) and silty sand (SM), respectively. To prepare the soil specimens, the soil was first air dried and then passed through a 2-mm sieve. The prepared soil was evenly spread on a steel plate and deionized water was sprayed onto the soil to increase its water content until

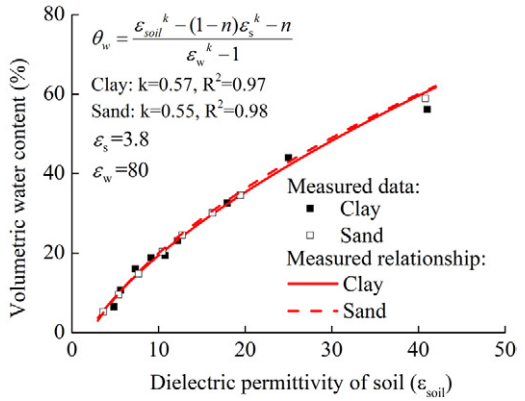

Fig. 6. Calibrated relationships between the dielectric permittivity and volumetric water content for clay and sand. ε_s is the dielectric permittivity of soil particles, ε_W is the dielectric permittivity of water, n is soil porosity, and k is the geometric factor.

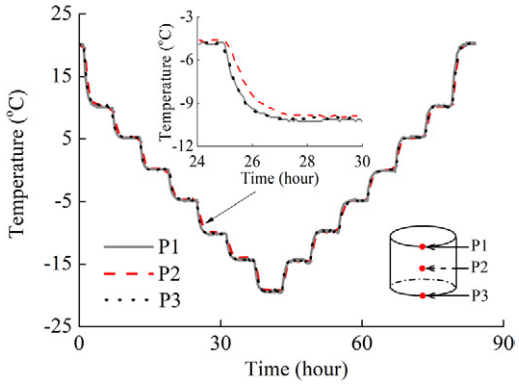

Fig. 7. Measured temperature distribution within soil specimen during a heating and cooling cycle.

Table 1. Physical properties of the test clay and sand.

Parameters	Clay (Ng et al., 2017)	Sand
Specific gravity	2.69	2.67
Liquid limit, %	36	–
Plastic limit, %	19	–
Plasticity index, %	17	–
Unified Soil Classification System	Lean clay (CL)	Silty sand (SM)

a gravimetric water content of 9.2% was reached. The mixture was again passed through the 2-mm sieve to reduce soil clod size, then transferred to and stored in a sealed plastic bag for 4 d for moisture equalization. Cylinder specimens, which are 76 mm in diameter and 30 mm in height, were compacted by three layers in a split mold. The target dry density of the soil specimens was 1.18 g cm^{-3}.

Test Program and Procedures

Five temperature-controlled triaxial tests were conducted to measure the SFCC of saturated soil specimens at different confining stresses. The stresses considered were 30, 100, and 200 kPa. A minimum confining stress of 30 kPa was applied to ensure that soil specimen was always in contact with the noninvasive TDR probe. More details about the test program are given in Table 2.

Each test consisted of three stages: saturation, consolidation, and freezing and thawing. The clay specimens were prepared using the method of static compaction. The initial void ratio after compaction is 1.09 and the initial dry density is 1.18 g cm^{-3}, which corresponds to a relative compaction of 75%. During the compression to 30, 100, and 200 kPa, void ratio of these specimens reduced to 1.08, 0.88, and 0.78, respectively. The measured relations between void ratio and stress are consistent with those reported by Ng et al. (2018). On the other hand, the sand specimens were statically compacted to the same initial void ratio as the clay specimens for comparing the SFCCs of these two materials. Upon the application of confining pressure, void ratio reduced to 1.06 and 1.05 at 30 and 200 kPa, respectively. The relationships between stress and void ratio are consistent with the compression curve of a loose sand, which has a similar particle size distribution (Pestana and Whittle, 1995). After consolidation, the temperature of each specimen was decreased from 0 to −10°C in steps of 0.5°C at a constant confining stress. The ice nucleation of the pore water occurs in a relatively small temperature range because of supercooling. To measure SFCCs accurately, a small interval of thermal loading (0.5°C) was applied during the freezing. For the subsequent thawing, the pore ice was expected to thaw gradually with an increase in soil temperature. Therefore, a large thermal loading interval of 1°C was set during the thawing to shorten the experimental duration. It should be noted that the soil temperature is directly recorded through the thermocouples attached to the soil specimen, but not the temperature in the thermostat. The unfrozen water content of the soil specimen was measured with the noninvasive TDR in the both freezing and thawing processes.

Table 2. Test program parameters.

Test series	Test material	Confining stress	Void ratio, e_0 (initial state)	Void ratio, e_1 (after consolidation)
		kPa		
I	Clay	30	1.172	1.082
		100	1.168	0.878
		200	1.177	0.780
II	Sand	30	1.068	1.063
		200	1.071	1.055

Experimental Results

Stress Effects on the Soil Freezing Characteristic Curve

Clay under Freezing and Thawing

Figure 8 shows the measured SFCCs of clay at confining stresses of 30, 100, and 200 kPa. For the soil specimen at a confining stress of 30 kPa, the unfrozen volumetric water content is almost constant at temperatures ranging from 0 to −2°C. This is because that all soil water is able to retain liquid state because of the presence of metastable nucleation (Zhang et al., 2015). When soil temperatures further decrease from −2 to −10°C, the unfrozen water content decreases dramatically. During the subsequent thawing, the SFCC is almost flat at temperatures ranging from −10 to −1°C. When soil temperatures further increases from −1 to 0°C, a steep increase in the unfrozen volumetric water content is observed. On the other hand, there is a marked hysteresis loop between freezing and thawing curves of SFCC. The hysteresis of SFCC was also observed in previous experimental studies (Bittelli et al., 2003; Tian et al., 2017). According to the SFCC model developed by Mu et al. (2018), the capillary pressure at the ice–water interface (u_i–u_w, where u_i and u_w are the ice and water pressures, respectively) increases when soil temperature decreases. Water in a given pore would freeze when the capillary pressure increases to $2\sigma_{iw}\cos(\alpha)/r$, where σ_{iw}, α, and r are the surface tension coefficient, contact angle, and pore radius, respectively.

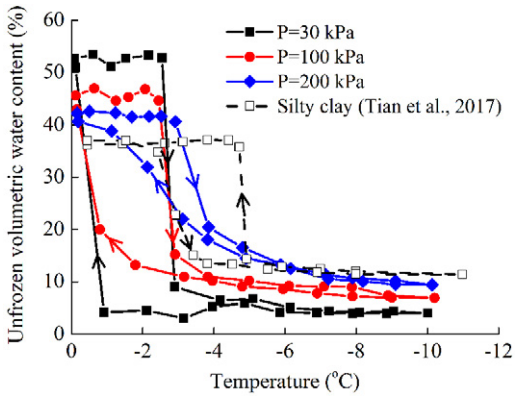

Fig. 8. Soil freezing characteristic curve (SFCCs) of clay subjected to freezing and thawing under confining stresses (P) of 30, 100, and 200 kPa.

The values of α are different along the freezing and thawing processes. A hysteresis between the freezing and thawing SFCCs is thus expected. On the other hand, the SFCC of a clay specimen obtained in the literature (Tian et al., 2017) is also included in the figure for comparisons. This result of SFCC was measured using the NMR technique without applying any stresses. During testing, the sample experienced three-dimensional freezing and thawing in a closed system, which is the same as the thermal loading condition adopted in this study. It can be seen that the SFCCs measured by Tian et al. (2017) show similar nonlinear patterns together with a similar hysteresis loop between the freezing and thawing curves. At a given temperature, the different unfrozen water retention capacities between their soil and the clay specimen tested in this study are probably due to different soil properties (e.g., specific surface area) and soil states (e.g., density).

For the clay specimens at confining stresses of 100 and 200 kPa, the measured SFCCs are qualitatively similar to that at 30 kPa. At a quantitative level, the unfrozen water content at 200 kPa is much larger than that at 100 and 30 kPa at temperatures ranging from −3 to −10°C during freezing and temperatures ranging from −10 to −1°C during thawing. On the other hand, the size of hysteresis loop decreases with increasing stresses. It clearly shows that the unfrozen water retention capacity of clay increases with increasing confining stresses. As explained above, the phase change between ice and water within a soil specimen can be described using the theory of capillarity (Tian et al., 2017; Mu et al., 2018). The void ratio of clay decreases by 33.7% when confining stress increases from 30 to 200 kPa (see Table 2), inducing a significant reduction of soil pore size. With a reduction of pore size, the capillarity is enhanced according to the Young–Laplace equation and hence soil specimen is able to retain more water at liquid state.

Figure 9 shows the changes in the void ratio of clay specimens during freezing and thawing. The soil void ratio at a given negative temperature is defined as the ratio of the volume occupied by liquid water and ice to that of soil particles [$e_T = (10e_0 - \theta_{wT})/(9 + \theta_{wT})$, where e_0 and θ_{wT} are the initial soil void ratio and the unfrozen volumetric water content at a given negative temperature, respectively].

The void ratios of all clay specimens increase when the liquid water is frozen, whereas the thawing of the pore ice induces a decrease in the soil void ratio. It should be noted that the density of liquid water (1.0 g cm^{-3}) is ∼1.1 times larger than that of ice. Therefore, the freezing of liquid water and the thawing of ice would cause the expansion and contraction of clay specimens, respectively. In addition, the patterns of the changes in soil void ratio with temperature are similar to that of SFCCs.

Sand under Freezing and Thawing

Figure 10 shows the measured SFCCs of sand at confining stresses of 30 and 200 kPa. The SFCC of sand tested by Tian et al. (2017) using the NMR technique is also included in the figure for comparisons. Similar patterns of SFCCs were determined through the NMR technique and the TDR method. It proves the efficiency of the newly developed triaxial apparatus in this study. On the other hand, for the sand specimens at confining stresses of 30 and 200 kPa, the measured SFCCs generally share similar patterns to that of clay specimens during both freezing and thawing processes. The ice nucleation and ice melting mainly occurs in the temperatures ranging from −2 to −3°C during freezing and temperatures ranging from −1 to 0°C during thawing, respectively. The hysteretic behavior of the measured SFCC is also observed in sand specimens at confining stresses of 30 and 200 kPa. Similar explanations for the freezing and thawing hysteresis loop of clay (e.g., pore size irregularities) could also apply to the sand specimens. More importantly, stress effects on SFCCs and its hysteresis loop of sand specimens are much smaller than those of clay specimens. This is probably because that the stress-induced change in pore size distribution is smaller in sand due to its smaller compressibility (Cui et al., 2016). As shown in Table 2, the void ratio of sand only decreases by 1.5% with increasing the confining stress from 30 to 200 kPa. The enhancement of capillarity by the confining stress is not as significant as clay.

Figure 11 shows the changes in the void ratio of sand specimens under freezing and thawing. The determination of the void ratio of sand specimens at each of temperature step is similar to the method described in the Fig. 9. The void ratios of sand specimens

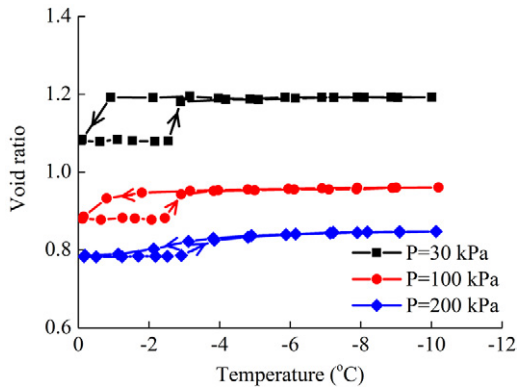

Fig. 9. Changes in void ratios for clay specimens subjected to freezing and thawing under confining stresses (P) of 30, 100, and 200 kPa.

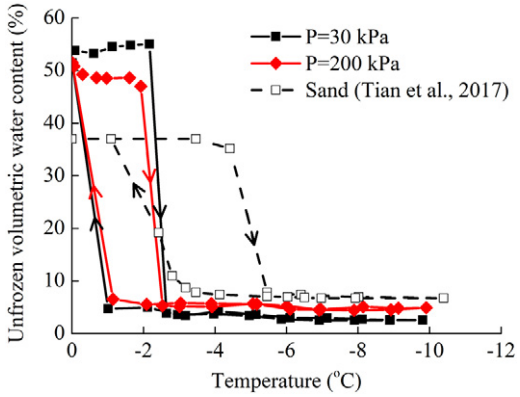

Fig. 10. Soil freezing characteristic curve (SFCCs) of sand subjected to freezing and thawing under confining stresses (P) of 30 and 200 kPa.

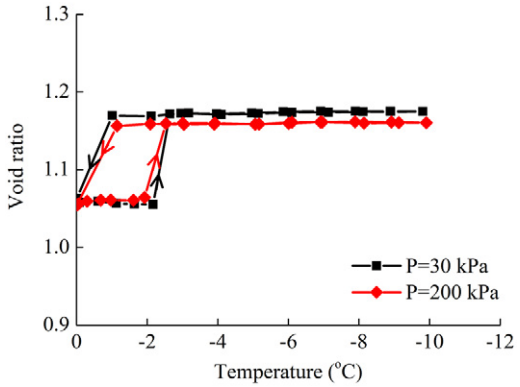

Fig. 11. Changes in void ratios for sand specimens subjected to freezing and thawing under confining stresses (P) of 30 and 200 kPa.

also increase when the ice nucleation occurs, whereas the thawing induces a decrease in the soil void ratio. Similar to clay specimens, the changes in the void ratio of sand specimens with temperature could also be explained by the density differences between ice and liquid water.

Summary and Conclusions

In this study, a new stress- and temperature-controlled triaxial apparatus was developed for measuring SFCC at various confining stresses. The unfrozen water content was determined using a new noninvasive TDR probe installed in the top cap. Calibration tests show that dielectric permittivity measured by the noninvasive TDR probe is highly related to soil water content (i.e., $R^2 > 0.97$). The new apparatus was used to measure SFCCs of two typical soils (i.e., clay and sand) at different confining pressures. The following conclusions can be drawn:

1. Thickness of the circuit laminate installed in the top cap strongly affects sample area of the noninvasive TDR probe. For the new triaxial apparatus, a thickness of 6 mm is able to ensure almost constant sample area and to eliminate the influence of sample area on sensor responses.
2. With an increase in confining pressure, both clay and sand are able to retain more pore water at liquid state. This is mainly because that the capillarity is enhanced due to stress-induced compression. The above finding implies that the conventional method without stress control would overestimate the ice content and shear strength of frozen soils.
3. Stress effects on the SFCC of sand are much less significant than that of clay. It is because the stress-induced change in pore size distribution of sand is much smaller than that of clay, so that the stress-induced enhancement of capillarity for sand is less significant.

Acknowledgments

We would like to acknowledge the financial support provided by the Key Research Program of Frontier Sciences, Chinese Academy of Sciences (CAS) (Grant no. QYZDB-SSW-DQC010), the Youth Innovation Promotion Association CAS, the Research Grants Council of the Hong Kong Special Administrative Region (HKSAR) (Grant no. 16204817 and AoE/E-603/18), the Innovative Talents Promotion Plan in Shaanxi Province, China (Grant no. 2018KJXX-033), the China Postdoctoral Science Foundation (Grant no. 2018M631166), and the Fundamental Research Funds for the Central Universities of China (Grant no. xjj2018250).

References

Al-Raoush, R., and A. Papadopoulos. 2010. Representative elementary volume analysis of porous media using X-ray computed tomography. Powder Technol. 200:69–77. doi:10.1016/j.powtec.2010.02.011

Archer, D.G., and P. Wang. 1990. The dielectric constant of water and Debye-Hückel limiting law slopes. J. Phys. Chem. Ref. Data 19:371–411. doi:10.1063/1.555853

ASTM. 2011. ASTM D 2487-11: Standard practice for classification of soils for engineering purposes (Unified Soil Classification System). ASTM Int., West Conshohocken, PA.

Azmatch, T.F., D.C. Sego, L.U. Arenson, and K.W. Biggar. 2012. Using soil freezing characteristic curve to estimate the hydraulic conductivity function of partially frozen soils. Cold Reg. Sci. Technol. 83–84:103–109. doi:10.1016/j.coldregions.2012.07.002

Birchak, J., C. Gardner, J. Hipp, and J. Victor. 1974. High dielectric constant microwave probes for sensing soil moisture. Proc. IEEE 62:93–98. doi:10.1109/PROC.1974.9388

Bittelli, M., M. Flury, and G.S. Campbell. 2003. A thermodielectric analyzer to measure the freezing and moisture characteristic of porous media. Water Resour. Res. 39:1041. doi:10.1029/2001WR000930

Cui, Y., A. Nouri, D. Chan, and E. Rahmati. 2016. A new approach to the DEM simulation of sand production. J. Petrol. Sci. Eng. 147:56–67. doi:10.1016/j.petrol.2016.05.007

Ferré, P.A., J.H. Knight, D.L. Rudolph, and R.G. Kachanoski. 1998. The sample areas of conventional and alternative time domain reflectometry probes. Water Resour. Res. 34:2971–2979. doi:10.1029/98WR02093

Flerchinger, G.N., M.S. Seyfried, and S.P. Hardegree. 2006. Using soil freezing characteristics to model multi-season soil water dynamics. Vadose Zone J. 5:1143–1153. doi:10.2136/vzj2006.0025

He, H., and M. Dyck. 2013. Application of multiphase dielectric mixing models for understanding the effective dielectric permittivity of frozen soils. Vadose Zone J. 12(1). doi:10.2136/vzj2012.0060

Knight, J.H. 1992. Sensitivity of time domain reflectometry measurements to lateral variations in soil water content. Water Resour. Res. 28:2345–2352. doi:10.1029/92WR00747

Konrad, J.M. 1990. Unfrozen water as a function of void ratio in a clayey silt. Cold Reg. Sci. Technol. 18:49–55. doi:10.1016/0165-232X(90)90037-W

Lebeau, M., and J.M. Konrad. 2012. An extension of the capillary and thin film flow model for predicting the hydraulic conductivity of air-free frozen porous media. Water Resour. Res. 48:W07523. doi:10.1029/2012WR011916

Lin, C.P., S.H. Tang, and C.C. Chung. 2006. Development of TDR penetrometer through theoretical and laboratory investigations: 1. Measurement of soil dielectric permittivity. Geotech. Test. J. 29:306–321.

Mu, Q.Y., C.W.W. Ng, C. Zhou, G.G.D. Zhou, and H.J. Liao. 2018. A new model for capturing void ratio-dependent unfrozen water characteristics curves. Comput. Geotech. 101:95–99. doi:10.1016/j.compgeo.2018.04.019

Ng, C.W.W., Q. Cheng, and C. Zhou. 2018. Thermal effects on yielding and wetting-induced collapse of recompacted and intact loess. Can. Geotech. J. 55:1095–1103. doi:10.1139/cgj-2017-0332

Ng, C.W.W., Q.Y. Mu, and C. Zhou. 2017. Effects of soil structure on the shear behaviour of an unsaturated loess at different suctions and temperatures. Can. Geotech. J. 54:270–279. doi:10.1139/cgj-2016-0272

Ng, C.W., and Y.W. Pang. 2000. Experimental investigations of the soil-water characteristics of a volcanic soil. Can. Geotech. J. 37:1252–1264. doi:10.1139/t00-056

Nissen, H.H., P.A. Ferré, and P. Moldrup. 2003. Metal-coated printed circuit board time domain reflectometry probes for measuring water and solute transport in soil. Water Resour. Res. 39:1184. doi:10.1029/2000WR000168

Pestana, J.M., and A.J. Whittle. 1995. Compression model for cohesionless soils. Geotechnique 45:611–631. doi:10.1680/geot.1995.45.4.611

Razavi, M.R., B. Muhunthan, and O. Al Hattamleh. 2006. Representative elementary volume analysis of sands using X-ray computed tomography. Geotech. Test. J. 30:212–219.

Roth, K., R. Schulin, H. Flühler, and W. Attinger. 1990. Calibration of time domain reflectometry for water content measurement using a composite dielectric approach. Water Resour. Res. 26:2267–2273.

Selker, J.S., L. Graff, and T. Steenhuis. 1993. Noninvasive time domain reflectometry moisture measurement probe. Soil Sci. Soc. Am. J. 57:934–936. doi:10.2136/sssaj1993.03615995005700040009x

Seyfried, M.S., and M.D. Murdock. 1996. Calibration of time domain reflectometry for measurement of liquid water in frozen soils. Soil Sci. 161:87–98. doi:10.1097/00010694-199602000-00002

Spaans, E.J., and J.M. Baker. 1995. Examining the use of time domain reflectometry for measuring liquid water content in frozen soil. Water Resour. Res. 31:2917–2925. doi:10.1029/95WR02769

Tian, H., C. Wei, Y. Lai, and P. Chen. 2017. Quantification of water content during freeze–thaw cycles: A nuclear magnetic resonance based method. Vadose Zone J. 17:160124. doi:10.2136/vzj2016.12.0124

Tian, Z., J. Heitman, R. Horton, and T. Ren. 2015. Determining soil ice contents during freezing and thawing with thermos-time domain reflectometry. Vadose Zone J. 14(8). doi:10.2136/vzj2014.12.0179

Watanabe, K., and T. Wake. 2009. Measurement of unfrozen water content and relative permittivity of frozen unsaturated soil using NMR and TDR. Cold Reg. Sci. Technol. 59:34–41. doi:10.1016/j.coldregions.2009.05.011

Zhan, L.T., Q.Y. Mu, Y.M. Chen, and R.P. Chen. 2013. Experimental study on applicability of using time-domain reflectometry to detect NAPLs contaminated sands. Sci. China Technol. Sci. 56:1534–1543. doi:10.1007/s11431-013-5211-8

Zhan, L.T., Q.Y. Mu, Y.M. Chen, and H. Ke. 2015. Evaluation of measurement sensitivity and design improvement for time domain reflectometry penetrometers. Water Resour. Res. 51:2994–3006. doi:10.1002/2014WR016341

Zhang, L., W. Ma, and C. Yang. 2015. Pore water pressure changes of supercooling and ice nucleation stages during freezing point testing. Géotech. Lett. 5:39–42.

Zhang, Y., and R.L. Michalowski. 2015. Thermal-hydro-mechanical analysis of frost heave and thaw settlement. J. Geotech. Geoenviron. Eng. 141:04015027. doi:10.1061/(ASCE)GT.1943-5606.0001305

Zhou, C., and C.W.W. Ng. 2014. A new and simple stress-dependent water retention model for unsaturated soil. Comput. Geotech. 62:216–222. doi:10.1016/j.compgeo.2014.07.012

Zhou, C., and C.W.W. Ng. 2016. Simulating the cyclic behaviour of unsaturated soil at various temperatures using a bounding surface model. Geotechnique 66:344–350. doi:10.1680/jgeot.15.P.001

Zhou, J., C. Wei, Y. Lai, H. Wei, and H. Tian. 2018. Application of the generalized Clapeyron equation to freezing point depression and unfrozen water content. Water Resour. Res. 54:9412–9431. doi:10.1029/2018WR023221